# VISION BASED JOINT ANGLE ESTIMATION OF ROBOTIC PLASMA MEDICINE DEVICES

A Thesis

by

TAIMOOR DAUD KHAN

Submitted to the Office of Graduate and Professional Studies of
Texas A&M University
in partial fulfillment of the requirements for the degree of

MASTER OF SCIENCE

| | |
|---|---|
| Chair of Committee, | Seok Chang Ryu |
| Committee Members, | Srikanth Saripalli |
| | Hangue Park |
| Head of Department, | Andreas A. Polycarpou |

August 2019

Major Subject: Mechanical Engineering

# ABSTRACT

This study proposes a vision-based algorithm for joint angle estimation of robotic plasma medicine devices with a steerable tip joint. The algorithm uses ArUco markers of size 4x4 because of their robust and fast detection. An ArUco marker with a square length of 9mm is attached to each of the rigid distal and proximal parts of the robot with respect to the tip joint connecting those parts, and the joint angle is measured using a high-definition (HD) webcam simulating an endoscope camera. The proposed vision-based method can eliminate the need for any additional physical sensors that increase the device size, and the approach is also free of any interference from the electromagnetic field generated by plasma, and the risk of electrical breakdown, which can disturb and potentially damage other sensors with conducting components.

The performance of the ArUco markers is explored in terms of the angle accuracy and precision with respect to other approaches such as electromagnetic (EM) position and orientation sensors and the kinematics model of the joint. Subsequently, the ArUco marker-based vision system is tested with real-time joint angle estimation for the continuous motion of the distal tip. The results from this series of experimental studies serve to validate the effectiveness of the proposed marker-based vision system as a feedback sensing component for the robot-assisted plasma medicine devices.

# DEDICATION

To my parents,

*Abdul Wahid Khan & Farzana Wahid.*

And to the men and women in science, who have dedicated their lives to understanding the intricate complexities of our universe.

# ACKNOWLEDGMENTS

I would like to express my sincere gratitude to my advisor Dr. Seok Chang Ryu for his advise, counsel and continued support through this academic venture. I also thank Dr. Srikanth Saripalli at the J. Mike Walker '66 Department of Mechanical Engineering, Texas A&M University for helping me with computer vision applications for my research and Dr. Hangue Park at the Department of Electrical & Computer Engineering, Texas A&M University for his valuable time and suggestions on improving my work.

I would like to extend my thanks to Brooks Mckinney in the BioRobotics Laboratory at Texas A&M University for assisting me with plasma robotic devices for my experiments. Lastly, I would like to express my heartfelt gratitude to my friend and fellow Aggie Zaryab Shahid, for being my family away from home.

CONTRIBUTORS AND FUNDING SOURCES

## Contributors

This work was supported by a thesis committee consisting of Assistant Professor Seok Chang Ryu and Associate Professor Srikanth Saripalli of the Department of Mechanical Engineering, and Assistant Professor Hangue Park of the Department of Electrical and Computer Engineering. All work for the thesis was completed by the student, under the advisement of Seok Chang Ryu of the Department of Mechanical Engineering.

## Funding Sources

There are no outside funding contributions to acknowledge related to the research and compilation of this document.

# NOMENCLATURE

| | |
|---|---|
| NTP | Non Thermal Plasma |
| EM | Electromagnetic |
| FBG | Fiber Bragg Grating |
| MIS | Minimally Invasive Surgery |
| HD | High Definition |
| PnP | Perspective-n-Point |
| APPJ | Atmospheric Pressure Plasma Jet |
| RONS | Reactive Oxygen and Nitrogen Species |
| DOF | Degrees of Freedom |
| $D$ | Outer diameter of Plasma Robot |
| PTFE | PolyTetraFluoroEthylene |
| $r$ | Moment Arm of the Servo Motor |
| $\phi$ | Angle swept by the Servo Motor Shaft |
| $\Delta L$ | Change in Tendon Length |
| $\theta$ | Joint Angle |
| $l$ | Nominal Tendon Length |
| $l_1$ | Distance between the Joint Center and the edge of Proximal Link |
| $l_2$ | Distance between the Joint Center and the edge of Distal Link |
| fps | Frames per Second |
| ($k_1$, $k_2$, $k_3$) | Radial Distortion Coefficients |
| ($p_1$, $p_2$) | Tangential Distortion Coefficients |

| | |
|---|---|
| $(f_x, f_y)$ | Camera Focal Length |
| $(c_x, c_y)$ | Camera Optical Center |
| $m$ | Slope of the best fit line |
| $b$ | y intercept of the best fit line |
| $\bar{x}$ | Mean of the x-coordinates of the data points |
| $\bar{y}$ | Mean of the y-coordinates of the data points |
| $\overline{xy}$ | Mean of the product of the xy coordinates of the data points |
| $\overline{x^2}$ | Mean of the squares of the x-coordinates of the data points. |
| $R^2$ | Coefficient of Determination |
| $SE_{line}$ | Sum of squared errors of each data point from the corresponding predicted points on the regression line |
| $SE_y$ | Sum of squared errors of each data point from $\bar{y}$ |
| $\theta_d$ | Desired Joint Angle |
| $\Delta\theta$ | Difference between the desired and filtered joint angle |
| $\theta_f$ | Filtered Joint Angle |
| $\theta_t$ | True Joint Angle |
| $\theta_m$ | Measured Joint Angle |
| $u$ | Control Signal |

TABLE OF CONTENTS

Page

ABSTRACT ..... ii

DEDICATION ..... iii

ACKNOWLEDGMENTS ..... iv

CONTRIBUTORS AND FUNDING SOURCES ..... v

NOMENCLATURE ..... vi

TABLE OF CONTENTS ..... viii

LIST OF FIGURES ..... x

LIST OF TABLES ..... xii

1. INTRODUCTION ..... 1

2. BACKGROUND ..... 5

    2.1 Plasma Medicine Devices ..... 5
    2.2 ArUco Markers ..... 6

3. RESEARCH OBJECTIVES ..... 8

4. METHOD AND ANGLE ESTIMATION ALGORITHM ..... 10

5. ROBOT KINEMATICS ..... 12

6. EXPERIMENTS AND RESULTS ..... 17

    6.1 Experimental Setup ..... 17
        6.1.1 Plasma Robot ..... 17
        6.1.2 Camera ..... 18
        6.1.3 EM Sensor ..... 19
        6.1.4 Vector Graphics ..... 20
    6.2 Discretized Angle Measurements ..... 21
        6.2.1 Calibrated Kinematic Model ..... 26
    6.3 Real Time Continuous Angle Measurements ..... 30
    6.4 Angle measurements with an Active Plasma Plume ..... 32

7. CONCLUSION ..... 35

REFERENCES ..... 37

LIST OF FIGURES

FIGURE Page


1.1 Robotic Plasma Medicine Device ..... 2

2.1 ArUco Marker ..... 7

4.1 ArUco marker based joint angle estimation ..... 10

5.1 Plasma Robot Joint Kinematics. Joint moves from mean to the negative extreme and this is brought about by actuating Motor 1. ..... 14

5.2 Plasma Robot Joint Kinematics. Joint moves from positive extreme to the mean position and this is brought about by actuating Motor 1..... 15

6.1 Plasma robot with added square platforms and attached ArUco Markers. ..... 18

6.2 NDI Aurora V3 Electromagnetic Sensor. ..... 20

6.3 Experimental Setup for experiments 1 and 2..... 22

6.4 Discretized Angle Measurements, (a) Positive angle measurements and (b)Negative Angle measurements. ..... 23

6.5 Accuracy and Precision Assessment, (a) Error Plot and (b) Standard Deviation Plot. 25

6.6 Regression fits to positive angles subtended by Motor 2, (a) EM Sensor data and (b) Aruco Marker based Vision System data..... 27

6.7 Regression fits to negative angles subtended by Motor 1, (a) EM Sensor data and (b) Aruco Marker based Vision System data..... 28

6.8 Block diagram of the proposed control scheme for the plasma robot with an improved kinematic model..... 29

6.9 ArUco Marker tracking for Joint Angle Estimation, (a) 0°, (b)Positive extreme and (c)Negative extreme ..... 30

6.10 Continuous Real Time Joint Angle Measurements. ..... 31

6.11 Experimental Setup for experiment 3. ..... 32

6.12 Discretized Angle Measurements with an Active Plasma Plume ..... 33

6.13 Images for Vector Graphics approach (a) 35° and (b) -35 °. ..... 34

# LIST OF TABLES

TABLE Page

5.1 Summarized tendon based actuation ..... 13

6.1 Cube Volume (Planar Field Generator) - Orientation Errors ..... 21

6.2 Error Analysis of Discretized Angle Measurements ..... 24

# 1. INTRODUCTION

Plasma, in recent years, has been becoming increasingly popular in various medical procedures. The viability of using plasma, in particular, non-thermal plasma (NTP) for tissue regeneration, wound healing, cancer treatment, and various other medical conditions has been studied extensively [1]. However, the devices for plasma-mediated treatment require further engineering innovation; precise control systems and dose delivery mechanisms need to be developed for the clinical application of this technology.

To this end, in a recent work, researchers from our lab developed and validated the feasibility of an in vivo robotic plasma medicine device (see Fig 1.1 (a)), which can be used for treating exposed cancers inside of a human body in a minimally invasive way [2]. The device is designed to generate a stable plasma plume and is capable of delivering precisely controlled plasma doses to selectively kill tumors of various sizes. A steerable distal tip in the device design is intended to help it navigate to various deep-seated organs in the human body and to target normal-sized tumors at different orientations. But to dexterously maneuver the device, the joint angle between the distal and proximal parts need to be determined accurately. This joint angle measurement will serve as the feedback signal employed by the different close-loop control architectures for the precise positioning of the distal tip.

A popular way to determine joint angles in robot-assisted surgeries is to use position encoders. Position encoders are sensors consisting of a graduated scale and a read-head. The encoder determines the position of this read-head on the scale and outputs a voltage signal that is characteristic of the joint angle. Motorized joints in surgical robots use these encoders to complete the servo control loop [3] however, a motorized joint and an encoder at the proximal tip of our plasma medicine robot are susceptible to electromagnetic (EM) interference because of the EM fields generated by the plasma plume. For this reason, our device design uses a tendon actuated joint which is insusceptible to these EM fields. With a tendon-driven robot, one way to estimate the joint angle is to use a robot kinematic model [4]. Such a model correlates the joint angle with the change in

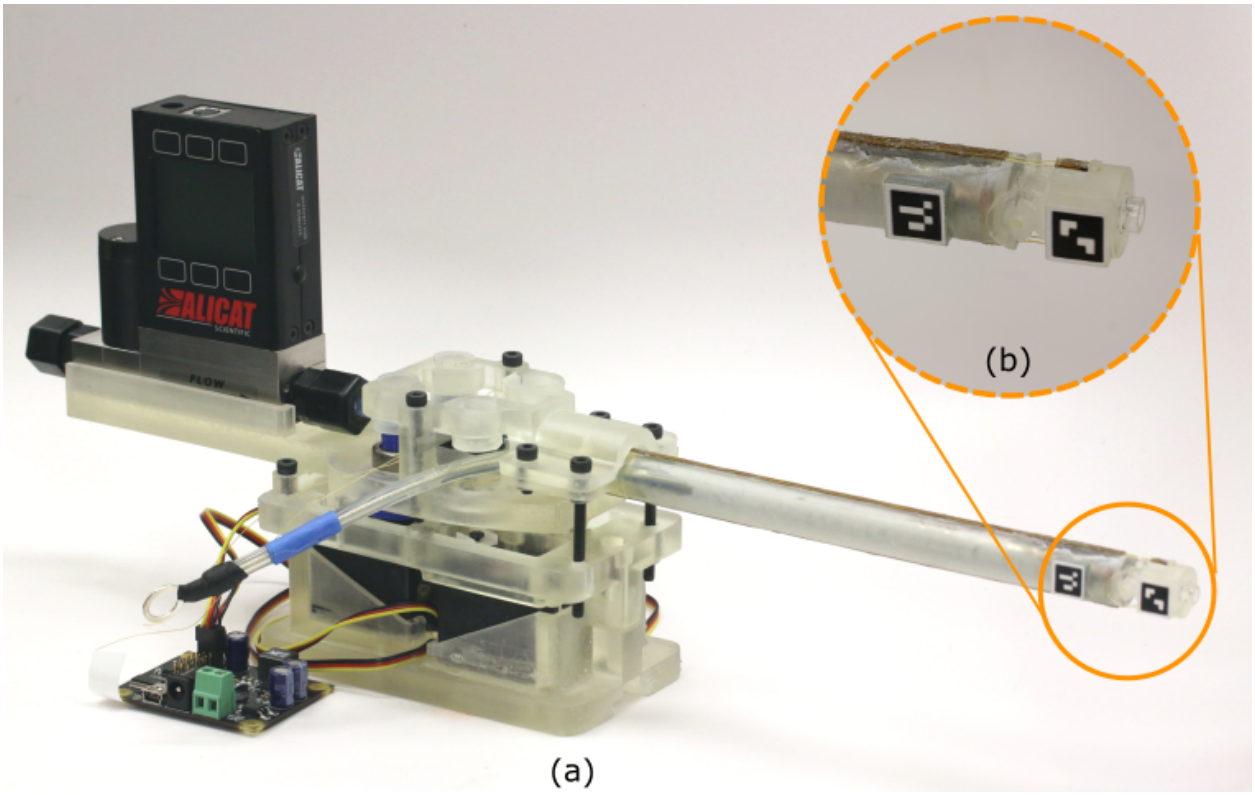


Figure 1.1: (a) The robotic plasma medicine device with the robotic interface and flow controller [2], and (b) Distinct ArUco markers placed at the proximal and distal segments of the device.

tendon length. These models, however, provide for only an open loop control system and are robot specific, that is they vary from one robot configuration to another. Also, these models rely on many assumptions about the tendons inelastic properties and the manner in which they are routed around the device. As such, these models are not the most accurate and hence fall short of providing the precision necessary to guide a plasma plume for cancer treatment. Another method to estimate the joint angles in surgical robots is to embed tiny electromagnetic (EM) sensors in the different links of the robot [5], [6]. These sensors are subjected to an EM field generated by a field generator and the resulting voltages then characterize the orientation of the segments housing these sensors. But like the position encoders in the motorized joints, these sensors are also sensitive to the EM fields generated by the plasma plume and hence, not suitable for use with our plasma robot. Another novel method for active tip steering of surgical devices that is robust to EM fields makes use of

optical strain sensors known as fiber Bragg gratings or FBGs [7]. These sensors are a popular choice with continuum manipulators in Minimally Invasive Surgery (MIS) and use the strain gage readings to estimate the needle curvature and position inside the human body. However, these strain sensors do not work well with high curvature needle bending or in our case with large distal tip angles. This is because the glass fiber breaks at these extremums and leads to a complete breakdown of the navigation system.

One way to circumvent the limitations of the aforementioned techniques is to use computer vision algorithms for joint angle estimation. These algorithms make use of the high definition (HD) endoscopic cameras used in robotic surgical procedures as an alternative real-time feedback sensor. In one example, to estimate the pose of instruments in the da Vinci Surgical System, researchers used region based methods with an estimated transform to position the vertices of the instruments CAD model in the camera frame and then generated silhouette regions from this projection. The pose was then estimated by matching the model silhouettes and the data silhouettes by pixel-wise classification [8]. Other methods in computer vision make use of different optical markers to ascertain the pose of an object. Markers composed of chessboard vertices and circular dots have been used for tracking ultrasonic probes in laparoscopic surgeries [9], [10]. And recently, hybrid markers comprising of a mixed pattern of both circular dots and chessboard vertices have also been suggested for pose estimation of ultrasonic probes in surgery [11]. Pose estimation from images of such markers is determined using the Perspective-n-Point (PnP) problem [12]. Recently, the PnP problem is being used with a new set of optical markers, called ArUco markers. These markers have also been used for pose and position estimation of various surgical tools and their support systems [13], [14], [15]. But this work has not yet been extended to joint angle estimation of articulated medical robots and plasma medicine devices.

In this paper, we propose a vision-based method with ArUco markers (see Fig 1.1 (b)) to determine the joint angles of articulated robotic plasma medicine devices. A further contribution of our work is in the performance evaluation of our proposed approach at a very small resolution. We validated and compared our results by using an electromagnetic sensor and a kinematic model

based on the change in the tendon pulling length. Our method is not susceptible to any EM fields and works well with plasma medicine devices. This method can also be applied to surgical tools in MIS and since it does not require any additional sensor it can be used to further miniaturize surgical instruments in MIS.

The proposed thesis document will be organized as follows, *Section II* presents background on our plasma medicine device and the proposed ArUco markers for the joint angle estimation. *Section III* describes the research objectives and the scope of our project. *Section IV* details the method and vision algorithm used for joint angle estimation and is followed by *Section V* which entails the plasma robots kinematic model. *Section VI* presents our experimental setup and evaluates the performance of our optical marker based approach with relevant discussions. Lastly, *Section VII* concludes the document with a summary of our key results and conclusions drawn from our work.

# 2. BACKGROUND

## 2.1 Plasma Medicine Devices

Non-thermal plasmas (NTPs), also known as atmospheric pressure plasma jets (APPJs) provide a rich source of reactive oxygen and nitrogen species (RONS) responsible for cytopathic effects in modern medicine. And their operation at atmospheric pressure and room temperature further motivates their medicinal use. However, plasma-mediated cancer treatment among deep-seated human body organs requires novel device designs for safe clinical applications. This necessity has motivated several academic circles to research safe and novel devices for channeling plasma to human organs. To this end, researchers have shown a successful generation of plasma at the tip of a long, flexible plastic tube using a thin metal wire installed inside the tube. This sort of setup allows for safe handling of the device without the risk of thermal or electric shocks but has several limitations. Plasma generation, gas discharge, and plume length are sensitive to conductive objects in contact with the tube wall. This, in turn, affects the stability of the plasma plume and the ability to control the dose for selective cancer treatment.

A viable solution to the shortcomings of contemporary plasma devices is to integrate with these devices the ability to selectively control the plasma dose. The proposed robotic plasma medicine device from our lab is capable of selective controlling plasma doses for cancer treatment and is equipped with a steerable distal tip. This steerable tip allows for dexterous manipulation of the device and helps with navigation about deep-seated organs. The steerable tip also allows small sized devices to target various normal sized tumors at different orientations. The experimental results evincing the performance of the device shows that it is devoid of thermal and electric failures and is safe for human touch. The robotic interface with tendon actuation allows for smooth motion of the distal tip and a flow regulator checks the dose of the plasma being delivered. To further improve the device design we look at different feedback sensing modalities for an effective control system design.

## 2.2 ArUco Markers

ArUco markers [16] are square markers that consist of a black border encompassing a grid of black and white squares (Fig 2.1(a)). The pattern of these black and white squares corresponds to a unique binary code and thus gives each marker a unique identity (Fig 2.2 (b)). ArUco marker dictionaries consist of markers of different sizes. The marker size $n$ refers to the size of the inner grid of squares i.e a marker with size $n = 4$ has an inner grid of size $4 \times 4$. The larger the marker size, the larger is the dictionary however with an increase in marker size, marker detection at longer distances becomes more difficult. For our application, a marker size of $n = 4$ suffices since our application does not require a large number of such markers. Also, a marker of this size is the aptest because of the small scale of contemporary medical devices.

ArUco marker detection is subject to its four corners being visible to the camera. The subsequent image processing steps include the application of adaptive thresholding to obtain borders, finding contours and filtering out unwanted or false borders. The filtering process removes borders with a small number of points, involves polygonal approximation and retains convex polygons with only four corners, and sorts the corners in an anticlockwise direction. This is followed by a marker identification step which involves using a homography transformation to get a normal view of the marker. The image processing algorithm then first checks the presence of a black border and then checks for and identifies the unique binary sequence encoded in the square grid. The final step is to refine the corners for valid markers by sub-pixel interpolation.

Pose estimation and position tracking using ArUco markers correspond to finding a homogeneous transform between two coordinates frames. These coordinate frames are the ones defined at the optical center of the image and at the center of the marker in the physical world. This transform can be found using the perspective n point (PnP) problem. For the PnP problem, the coordinates of the marker must be known in the frame attached to its center along with the coordinates of the markers projection on the image plane expressed in the frame fixed to the optical center. The latter coordinates are found via the image processing algorithm when detecting ArUco markers and marker coordinates in the physical world can be found by just specifying the markers physical

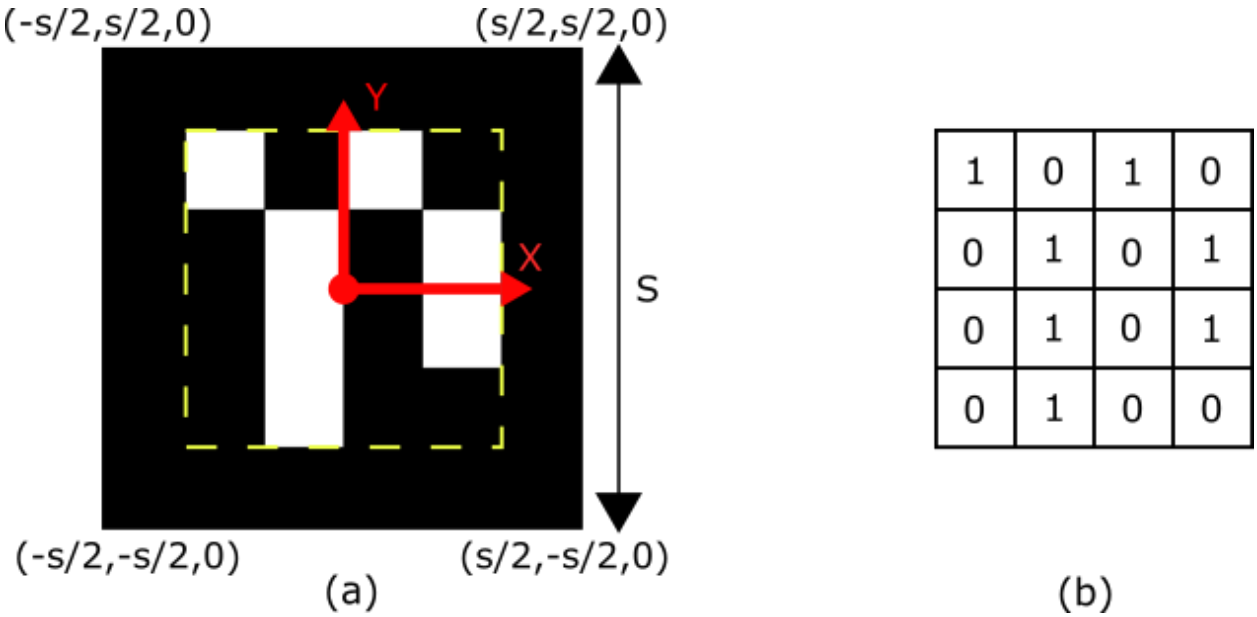


Figure 2.1: (a) ArUco Marker of size n=4, and (b) ArUco marker with the external border removed. The binary code represented by the black and white squares is shown in the grid.

size $s$. The PnP solution gives us a translation vector and a rotation vector. The translation vector locates the marker with respect to the camera and the rotation vector specifies the orientation of the marker with respect to the camera.

# 3. RESEARCH OBJECTIVES

The crux of this study is to verify the feasibility of using a vision-based feedback approach for joint angle estimation of plasma medicine robots. A computer vision algorithm is developed for ArUco marker detection and joint angle estimation. This is followed by a derivation of the robot kinematic model as a function of the change in tendon length. A series of different experiments are performed, first to evaluate the performance of ArUco marker based angle estimation against a tendon kinematic model and a V3 Electromagnetic sensor, followed by the angle estimation in the presence of an active plasma plume. Subsequently, we present evidence of accurate and precise angle measurements from our optical marker based vision algorithm approach. As such the following research objectives corroborate our findings

1. Develop a method and vision algorithm for joint angle estimation

    (a) Method: derive a mathematical model using rotation matrices to determine the relative angle between the proximal and distal part.

    (b) Vision Algorithm: develop a code for marker detection and pose estimation using the PnP problem.

2. Evaluate the performance of marker-based vision algorithm

    (a) Accuracy Assessment: measure the joint angle from the vision algorithm and compare against measurements obtained from tendon kinematic model, EM sensor and vector graphics.

    (b) Precision Analysis: take repeated angle measurements for several distal tip angles. Calculate the mean and standard deviation for the measurements obtained for different angles to ascertain the precision of our method.

(c) Real-time joint angle estimation of Plasma robot: demonstrate the ability of our proposed method to estimate the joint angle in real time for continuous motion of the distal tip.

Given the objectives of our research, there are certain limitations to this study. First, the ArUco marker detection is subject to its four corners being visible to the camera. This means that if the marker gets occluded due to either roll of the device or because of blood smearing during the clinical application of this technology, this approach will fail. We investigate experimentally the extent of the field of view in which the marker is detectable and also discuss several possible future works that can resolve this issue. Another limitation is with respect to zero errors with the measurement systems when the joint angle is zero. This is due to errors in marker placement and EM sensor attachment. A mechanical stop is used to restrict the rotation at the joint and the joint angle is fixed at zero degrees. Zero errors are then measured for all measurement systems and all readings are subsequently adjusted.

# 4. METHOD AND ANGLE ESTIMATION ALGORITHM

We extend the PnP problem of finding the pose of markers with respect to the camera to finding the angle at the tip of the plasma medicine device. This involves attaching two different ArUco markers across a revolute joint of the plasma robot. The markers are attached such that their centers lie on a common axis when the joint angle is zero. We then solve the PnP problem for each individual marker and obtain two separate rotation and translation vectors (Fig. 4.1). Using the literature on 3D rotation we can then specify a rotation matrix that quantifies the 3D pose of one joint segment with respect to the other. This is given by the following relation

$$R = R_{proximal}^{T} * R_{distal} \tag{4.1}$$

where $R$ is the rotation matrix quantifying the pose of the distal section with respect to the proximal section, $R_{proximal}$ and $R_{distal}$ are the rotation matrices of distal section and the proximal section of the robot respectively.

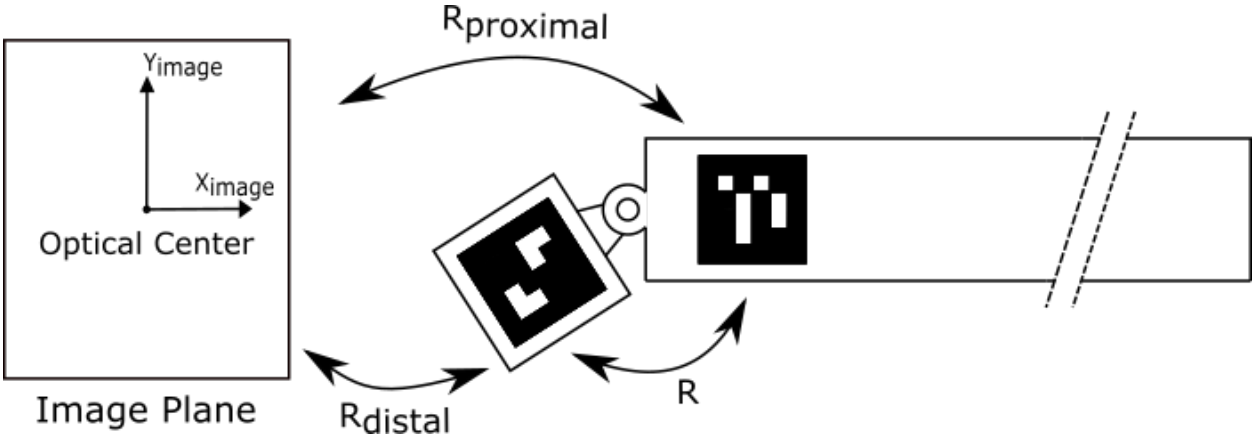


Figure 4.1: A schematic of the plasma medicine device with the attached ArUco markers of size n=4. Rotational matrices characterizing the orientation of each marker with respect to the camera frame are also shown.

We used C++ with OpenCV to write the image processing vision algorithm. The ArUco library is available with OpenCV which makes it easier and simpler to implement the aforementioned procedure. Algorithm 1 details the implementation of our image processing and angle estimation code. The highlighted text represents the coded method of our approach.

**Algorithm 1** Angle Estimation Algorithm

**Require:** Two distinct ArUco Markers

Specify ArUco Marker Dimension $s$
Declare a ptr to a predefined 4x4 dictionary
Declare a VideoCapture object
**if** !VideoCapture.isopened **then**
    exit
**end if**
**while** true **do**
    aruco::detectMarkers $\rightarrow$ markerCorners, markersIds
    aruco::estimatePoseSingleMarkers $\rightarrow$ rvec, tvec
    aruco::drawDetectedMarkers

    **for** i = 0; i $<$ markerIds.size(); i++ **do**
        **if** marekerIds[i]==30 **then**
            Rodrigues(rvec[i], $R_{proximal}$)
        **end if**
        **if** marekerIds[i]==42 **then**
            Rodrigues(rvec[i], $R_{distal}$)
        **end if**
        $R = R^T_{proximal} * R_{distal}$
    **end for**
    bool Rcheck = IsRotationMatrix($R$)
    **if** Rcheck == true **then**
        JointAngle = rotationMatrixtoEuler($R$)
    **end if**

**end while**

# 5. ROBOT KINEMATICS

The robotic plasma medicine device prototyped in our laboratory is a one degree of freedom (DOF) tubular structure with only two links. It consists of a single revolute joint and has an outer diameter $D$. The device is actuated using two kevlar tendons that run along the length of the robot on either side of the joint and are fastened to two separate servo motors. The tendons are routed along the device through PTFE composite tubing. We derived a tendon-robot kinematic model to be used as an input actuation map i.e. the desired joint angle at the robot tip is correlated with the servo motor angle. We also use this model for a comparative analysis with the joint angles determined from our vision algorithm. To estimate the joint angle we make use of the tendon pulling length and make the following set of assumptions

- The tendons are inelastic.
- The tendons are constrained along the entire length of the robot with a PTFE composite tubing except at the joint.
- The tendons are constrained in a 2-dimensional plane.
- The change in tendon length is observed only at the revolute joint.

With these assumptions, we can estimate the change in tendon length, $\Delta L$ as equivalent to the length of the arc swept by the moment arm of the servo motor to which the tendon is attached. Mathematically this is represented as

$$\Delta L = r\phi \tag{5.1}$$

where r is the moment arm of the servo motor and $\phi$ is the angle swept by the motor shaft. The derived mathematical function that correlates the joint angle, $\theta$ to change in tendon length, $\Delta L$ is found to be piecewise function. Considering the entire range of motion as the functional domain

of our derived model, it is split into two sub-domains; motion from mean position (i.e. when joint angle is zero) to either extreme (positive or negative) and motion from these extremums to the mean position. Mathematically this can be represented as

$$\theta = \begin{cases} f(\Delta L) & \text{if motion is from mean to extreme} \\ g(\Delta L) & \text{if motion is from extreme to mean} \end{cases} \tag{5.2}$$

The overall tendon actuation scheme with the two motors and the piecewise function is summarized in Table 1.

| **Tendon Based Actuation (Joint Motion)** | | |
|---|---|---|
| *Motor #* | *Tendon Kinematic Model* | |
| | f($\Delta l$) | g($\Delta l$) |
| 1 | mean to negative extremum | positive extremum to mean |
| 2 | mean to positive extremum | negative extremum to mean |

Table 5.1: Summarized tendon based actuation

We analyze the joint geometry for an arbitrary angle in these sub-domains to derive our model. To determine the function $f(\Delta L)$ we take a look at Fig. 5.1 which shows the joint kinematics for an arbitrary angle, $\theta$ when the tip moves from the mean position to the negative extreme. The figure also shows how the change in tendon length $\Delta$L appears at the joint at this joint angle $\theta$. When the joint angle is 0 °, there is no change in tendon length and the nominal tendon length at the joint is denoted as $l$. Now, to determine the angle $\theta$, we analyze the geometry shown in yellow in Fig. 5.1. Given the distance between the joint center and the edge of proximal link as $l_1$, and the distance between the joint center and the edge of distal link as $l_2$, we first determine the lengths $l_{be}$ and $l_{bd}$ using the Pythagorean theorem. Then using trigonometric relations we find the angles $\alpha$

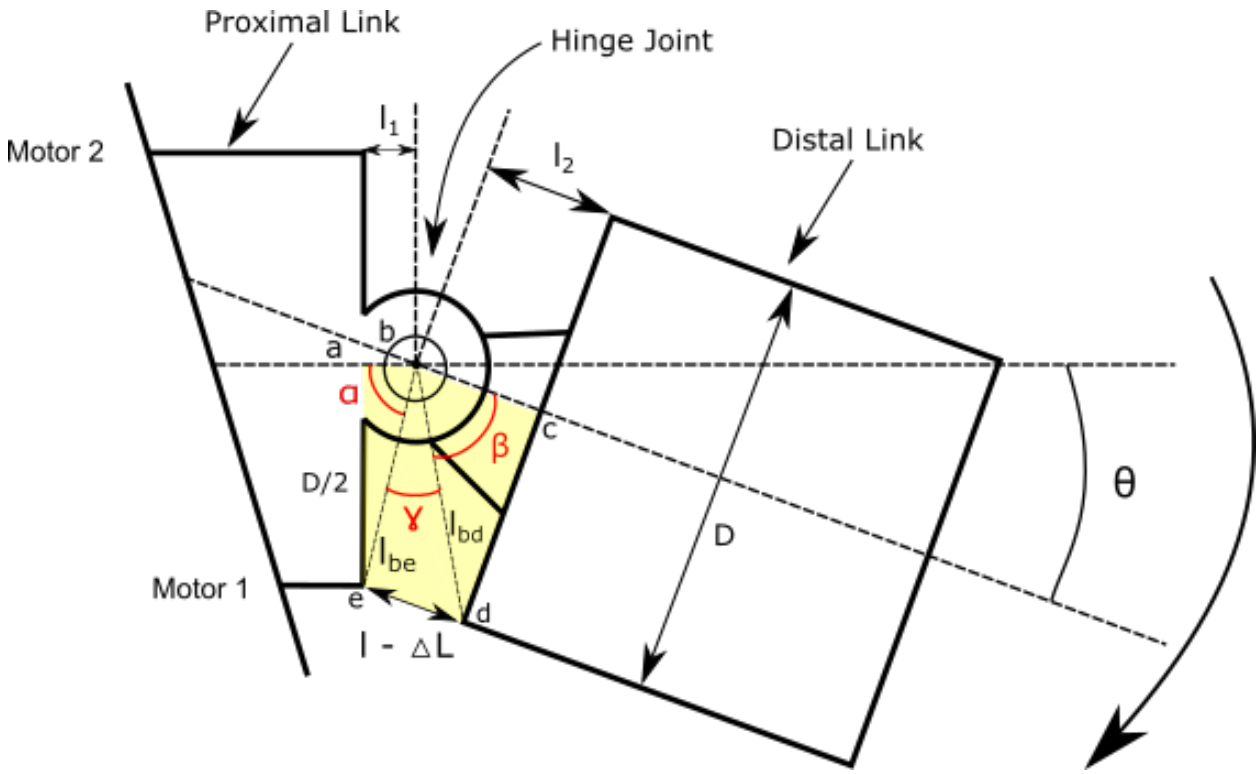


Figure 5.1: Plasma Robot Joint Kinematics. Joint moves from mean to the negative extreme and this is brought about by actuating Motor 1.

and $\beta$. And using cosine law and eq. 5.1 we then determine angle $\gamma$ from the following equation

$$\gamma = \arccos\left(\frac{l_{be}^2 + l_{bd}^2 - (l - \Delta L)^2}{2(l_{be})(l_{bd})}\right) \tag{5.3}$$

The function $f(\Delta L)$ is then simply calculated as

$$f(\Delta L) = \pi - (\alpha + \beta + \gamma) \tag{5.4}$$

The above relation also holds true for when the distal tip moves from the mean to the positive extremum. In this case, the tip is actuated by motor 2.

Similarly, to determine the function $g(\Delta L)$ we take a look at Fig. 5.2 which shows the joint kinematics for an arbitrary angle $\theta$ when the tip moves from the negative extremeum to the mean position. Notice how the change in tendon length $\Delta$L appears at the joint for this motion. The

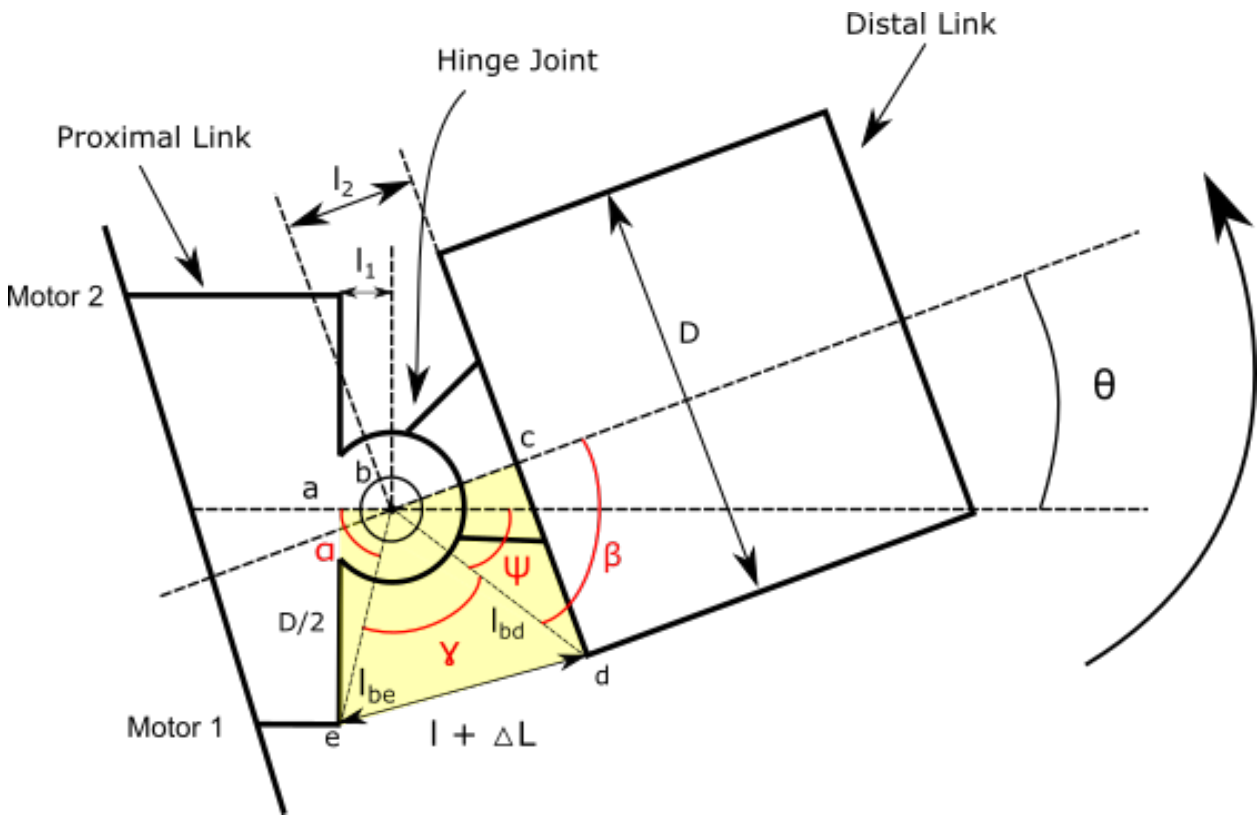


Figure 5.2: Plasma Robot Joint Kinematics. Joint moves from positive extreme to the mean position and this is brought about by actuating Motor 1.

change in tendon length gets added to the nominal tendon length $l$, unlike the previous case. Again, we analyze the geometry shown in yellow in Fig 5.2. Since $l_1$ and $l_2$ are robot design parameters, they remain unchanged and hence the lengths $l_{be}$ and $l_{bd}$ also remain unchanged. Consequently angles $\alpha$ and $\beta$ also remain the same. Using cosine law once again the varying angle $\gamma$ in Fig. 5.2. is then given as

$$\gamma = \arccos\left(\frac{l_{be}^2 + l_{bd}^2 - (l + \Delta L)^2}{2(l_{be})(l_{bd})}\right) \tag{5.5}$$

Using $\gamma$ we then calculate the other varying angle $\psi$ as

$$\psi = \pi - (\alpha + \gamma) \tag{5.6}$$

The function $g(\Delta L)$ which is then simply calculated as

$$g(\Delta L) = \beta - \psi \tag{5.7}$$

This relation also holds true for when the distal tip moves from the negative extreme to the mean position. In this case, the tip is actuated by motor 2.

The above kinematic model measures the servo angle for each motor as incremented from the servo angle at which the tendon is brought into tension when the joint angle is zero. This requires us to find the servo angle for each motor for which the tendon is taught when the corresponding angle subtended at the tip is $0°$.

# 6. EXPERIMENTS AND RESULTS

We worked with two experimental setups and performed three different sets of experiments to validate our proposed approach for joint angle estimation. The first of our two experimental setups was used to validate and compare the performance of our proposed method with other existing techniques. It did not involve any plasma plume generation as plasma interferes with the EM sensor validation setup. Two sets of experiment were carried with this setup. The second experimental setup was used to evaluate the performance of our vision algorithm with an active plasma plume. The details of our experimental studies are detailed as follows.

## 6.1 Experimental Setup

### 6.1.1 Plasma Robot

The robotic plasma medicine device shown in Fig 1.1 was modified and raised square platforms were added to the distal and proximal links near the revolute joint to attach the ArUco markers. The length of this square platform is 11 mm and the attached ArUco markers have a square dimension of 9 mm. ArUco marker attached to the proximal section has the Id 30 and that attached to the distal part has the Id 42. Fig. 6.1 shows the plasma robot with the square platform and the attached ArUco markers. In practice, any ArUco marker of size n=4 can be used and there are no restrictions on any specific marker Id.

Before running our experiments we eliminated any zero error between the pose of the two markers. This is because marker placement is done manually and so using our vision system we calculated the angle between two markers when the joint angle is zero. A mechanical bracket was 3D printed and was slid at the joint between the two links such that the joint was locked at 0° and then the zero error was measured. Ideally, this should be zero but taking into account the human error in marker placement we adjusted all subsequent angle measurements with this zero error value.

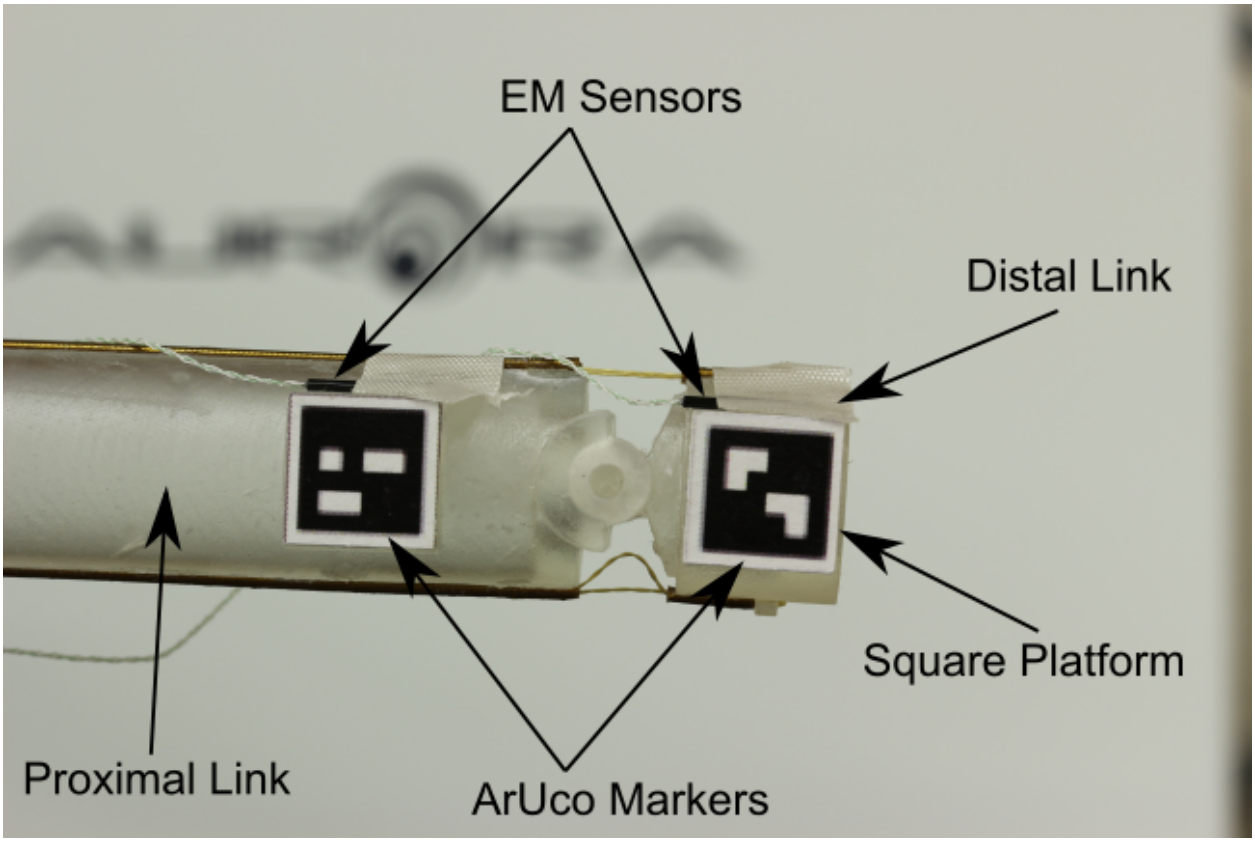


Figure 6.1: Plasma robot with added square platforms and attached ArUco Markers.

### 6.1.2 Camera

In our experiments, we used a Logitech BRIO Ultra HD Webcam for simulating an endoscope camera. This camera is rated at 30 fps (frames per second) when operated at 4K resolution and at 60 fps when operated at 1080p. When used with OpenCV at a 4K resolution the frame rate of this camera drops to 24 fps when no image processing is done. With our vision algorithm, this frame rate dropped further to approximately 6 fps (in actual it varies from 4 to 8 fps). The camera was mounted such that the focal plane was at an angle to the plasma robot and the attached markers. This was to realistically simulate the camera position in actual endoscopic surgeries. Before conducting the experiments we first performed a calibration of our camera using the ChArUco Board. ArUco markers on this board came from the dictionary DICT_6X6_250 and had a square dimension of 15.6 mm. Camera calibration is performed to eliminate any radial and tangential distortions

in the camera and to determine the intrinsic parameters of our camera. The distortion coefficients which characterize the radial and tangential distortions were determined to be as follows

$$Distortion\ Coeffiecients = \begin{bmatrix} k_1 \\ k_2 \\ p_1 \\ p_2 \\ k_3 \end{bmatrix} = \begin{bmatrix} 1.90 \\ -2.39 \\ 2.05 \\ -1.47 \\ -1.15 \end{bmatrix} \tag{6.1}$$

where, $k_1$, $k_2$ and $k_3$ are radial distortion coefficients and $p_1$ and $p_2$ are tangential distortion coefficients. The camera intrinsic parameters were found to be

$$Camera\ Matrix = \begin{bmatrix} f_x & 0 & c_x \\ 0 & f_y & c_y \\ 0 & 0 & 1 \end{bmatrix} = \begin{bmatrix} 748 & 0 & 317 \\ 0 & 749 & 249 \\ 0 & 0 & 1 \end{bmatrix} \tag{6.2}$$

where ($f_x$, $f_y$) represent the camera focal length and, ($c_x$, $c_y$) is the camera optical center. The average re-projection error for our calibration was determined to be 0.15 pixels which indicate a good camera calibration.

### 6.1.3 EM Sensor

We use an Aurora V3 EM sensor from NDI in our experiments. This is an advanced electromagnetic (EM) spatial measurement system. The sensor is used with the first of the two experimental setups that we used for experimental validation of our vision algorithm. The sensor is not used when experimenting with active plasma plume as EM fields from plasma generation interfere with the sensor readings. The sensor consists of the following components

- Planar Field Generator (FG)
- System Control Unit (SCU)
- Sensor Interface Unit (SIU)

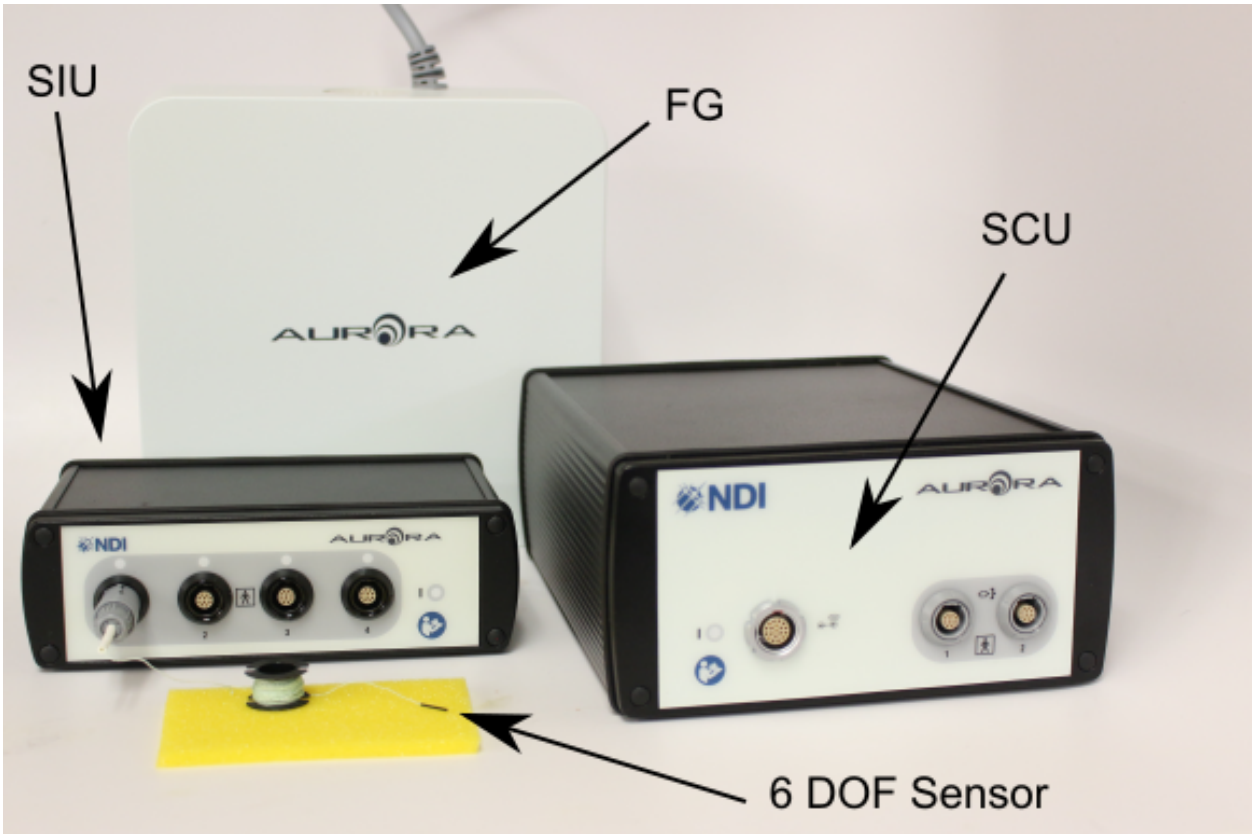


Figure 6.2: NDI Aurora V3 Electromagnetic Sensor.

- 6 DOF EM sensors (0.8 mm diameter x 9 mm)

The sensor components are shown in Fig. 6.2. The two 6 DOF EM sensors are attached to the proximal and distal links (see Fig. 6.1), with the sensor on the proximal part defined as our global reference standard. The pose between the two is then quantified with a quaternion which we then convert to an angle measurement.

In the two experiments with which we use this EM sensor, we consider it as our gold standard. This is because of the high accuracy and precision pertinent to this systems 6DOF sensor. The orientation errors for the system are detailed in Table 6.1.

### 6.1.4 Vector Graphics

To validate our vision algorithm in the presence of an active plasma plume we can not use the EM sensor so we used an off-line angle measurement technique. Since the robot is only 1 DOF

| Orientation Errors | 6 DOF | |
|---|---|---|
| | **RMS (°)** | **95% CI (°)** |
| *Orientation Accuracy* | 0.30 | 0.48 |
| *Orientation Precision* | 0.20 | 0.40 |
| *Orientation Trueness* | 0.25 | 0.45 |

Table 6.1: Cube Volume (Planar Field Generator) - Orientation Errors [17]

we mount a camera parallel to the motion plane in which the joint moves. For each discrete angle measurements, an image was captured which was then analyzed in a vector graphics software called Inkscape to get an estimate of the angle subtended at the robot tip. This technique was also extended to experiments that did not involve plasma generation.

### 6.2 Discretized Angle Measurements

The first set of experiments was conducted to investigate and compare the accuracy and precision of our proposed ArUco markers. For accuracy assessment, joint angle readings from ArUco marker-based vision system were compared against those obtained from the EM sensor, tendon kinematic model and from the vector graphics approach. For precision analysis for each joint angle, fifteen repeated readings were taken and the spread of the data analyzed. The experiment consisted of pulling the tendons for different displacements using two servo motors. These displacement correspond to unique joint angles as calculated from the kinematic model (-40°, -35°, -30°, -25°, -20°, -15°, -10°, -5°, 0°, 5°, 10°, 15°, 20°, 25°, 30°, 35°, 40°). The experimental setup for this experiment is shown in Fig. 6.3.

The results obtained for the discrete angle measurements are shown in Fig. 6.4. It is observed that the angle measurements from the ArUco marker-based vision system are very close to angle measurements from the EM sensor (our gold standard). The measurements from the vector graphics approach are also close to those obtained from the EM sensor however the error between the two is larger than the error between the ones obtained from our vision algorithm and the EM sensor. This may be because the image plane of the camera used for vector graphics approach is not exactly parallel to the motion plane. Please note that vector graphics is an off-line approach

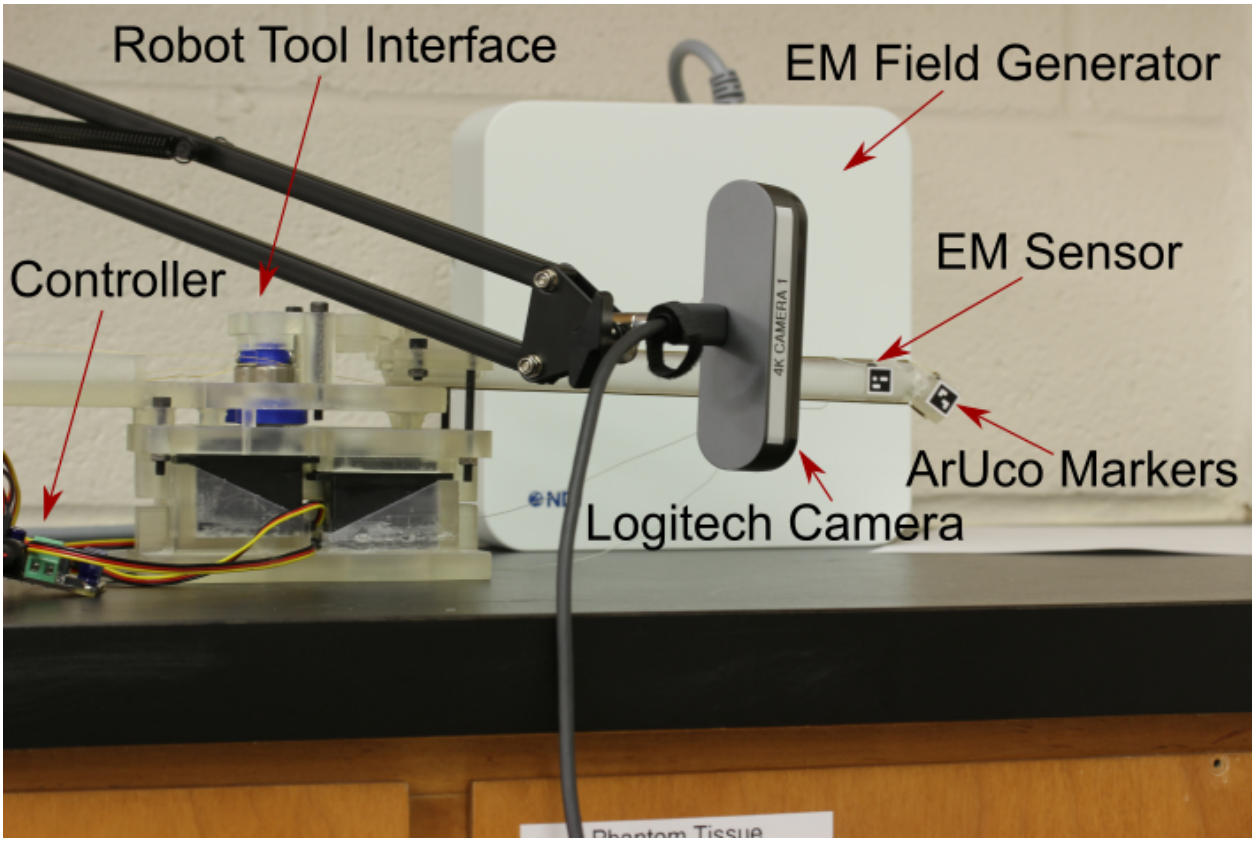


Figure 6.3: Experimental Setup for experiments 1 and 2.

with no feedback providing capabilities and was used only for validation. It is also prone to human error since when analyzing the images in Inkscape, the lines drawn parallel to the distal and proximal links may not be exact and slight inaccuracies can magnify the error in angle measurement. The tendon kinematic model performs the worst out of all measurement techniques and the error becomes especially large at larger angles (whether positive or negative). This is because the PTFE composite tubing is inaccurately placed. The tubing protrudes beyond the distal and proximal edge for tendons running along both sides of the robot. This protrusion alters the geometry shown in Fig. 5.1 and Fig. 5.2; the angles $\alpha$ and $\beta$ change. This coupled with the many assumptions that we made while deriving this model explains the poor performance of the tendon kinematic model. Another reason that might explain the poor performance of the tendon kinematic model is the controller issue. The kinematic model assumes that the servo actuation using the Phidget

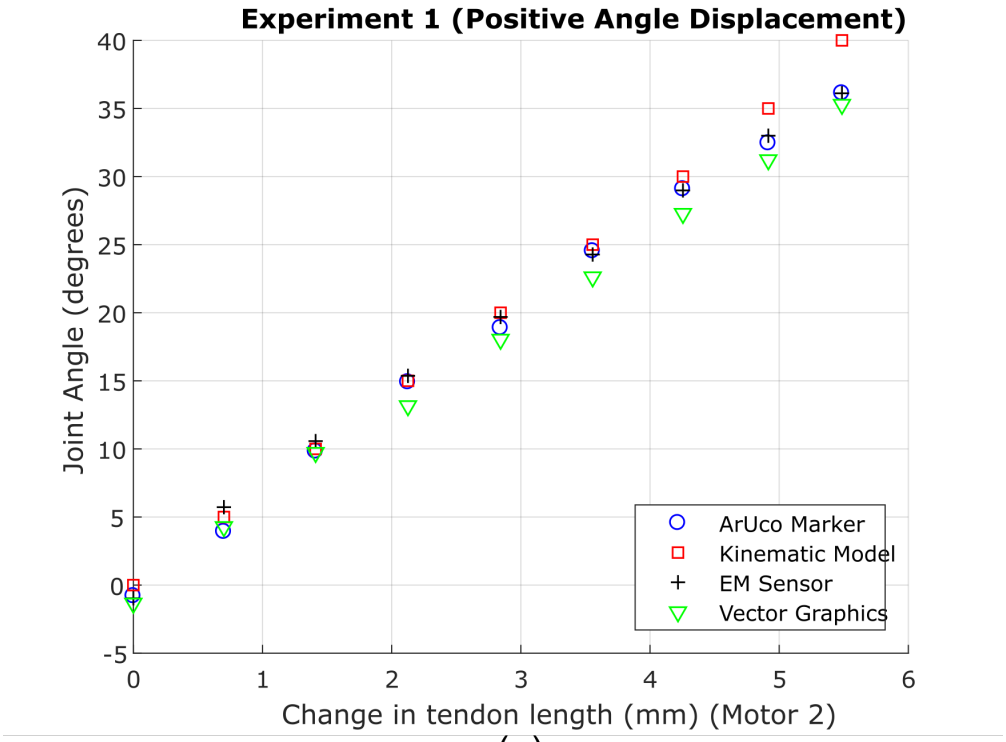


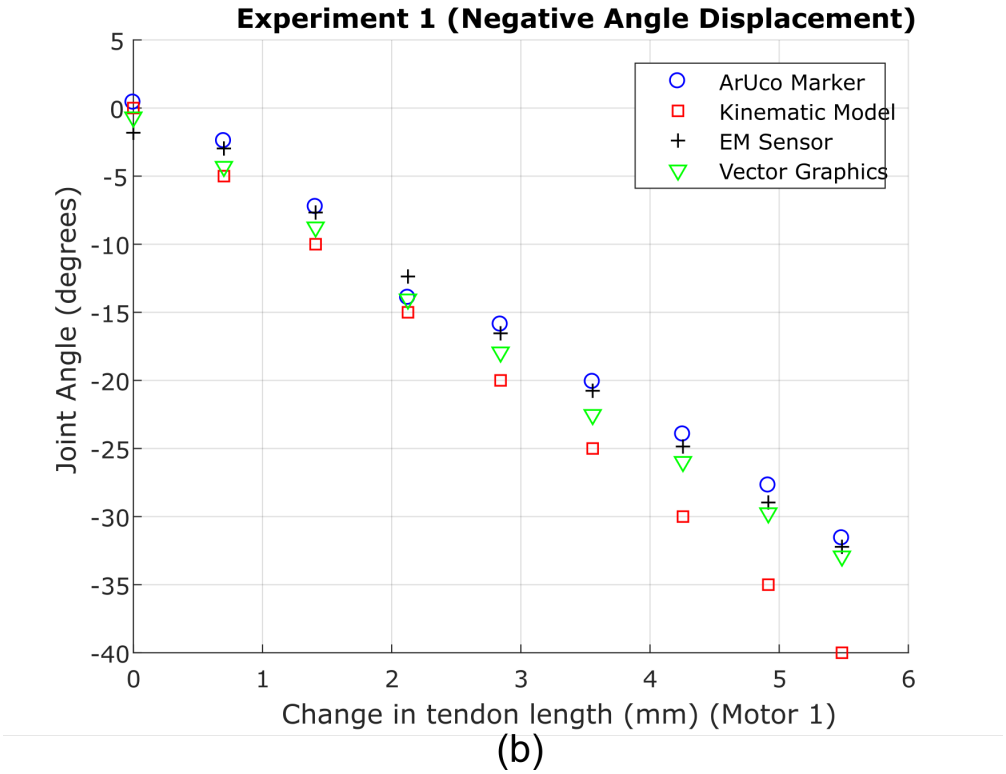


Figure 6.4: Discretized Angle Measurements, (a) Positive angle measurements and (b)Negative Angle measurements.

controller is accurate with no sources of error. If the controller is imprecise such that the servo angl,e $\phi$ subtended by the controller is different from the desired servo angle as calculated from the tendon kinematic model, the model will perform poorly.

To better ascertain the accuracy and precision assessment of our proposed approach we plotted the errors of our system with respect to the EM sensor and calculated the standard deviation of all 15 readings for each discretized angle. The results are shown in Fig. 6.5. The error plot (Fig. 6.5 (a)) shows that the error is roughly between $\pm$ 2° and that the maximum error is slightly above 2°. In fact, there are only three error values that exceed 1.5°. The standard deviation plot (Fig.6.5 (b)) shows that the maximum standard deviation value is about 2.2° and there are only three values that exceed a standard deviation of 1°. The overall error analysis for all measurement techniques is summarized in Table 6.2.

| **Error Analysis (in degrees)** | **Error Analysis w.r.t EM Sensor (Angle Measurement - EM Sensor Angle Measurement)** | | |
|---|---|---|---|
| | **Tendon Kinematics** | **Vector Graphics** | **Vision Algorithm** |
| **Absolute Max. Error** | 7.78 | 2.21 | 2.22 |
| **Absolute Min. Error** | 0.31 | 0.37 | 0.01 |
| **Mean** | -1.37 | -1.17 | 0.1 |
| **Standard Deviation** | 3.09 | 0.75 | 0.98 |
| **RMS Error** | 3.3 | 1.38 | 0.96 |

Table 6.2: Error Analysis of Discretized Angle Measurements

The table shows that the mean error for all set of discretized angles as measured by the ArUco marker-based approach is 0.1°, the lowest among all measurement techniques. Also, the RMS error is the lowest for the ArUco marker based angle estimation method. The maximum error is lowest for the vector graphics approach and it differs from the maximum error of marker-based vision algorithm approach by only 0.01°.

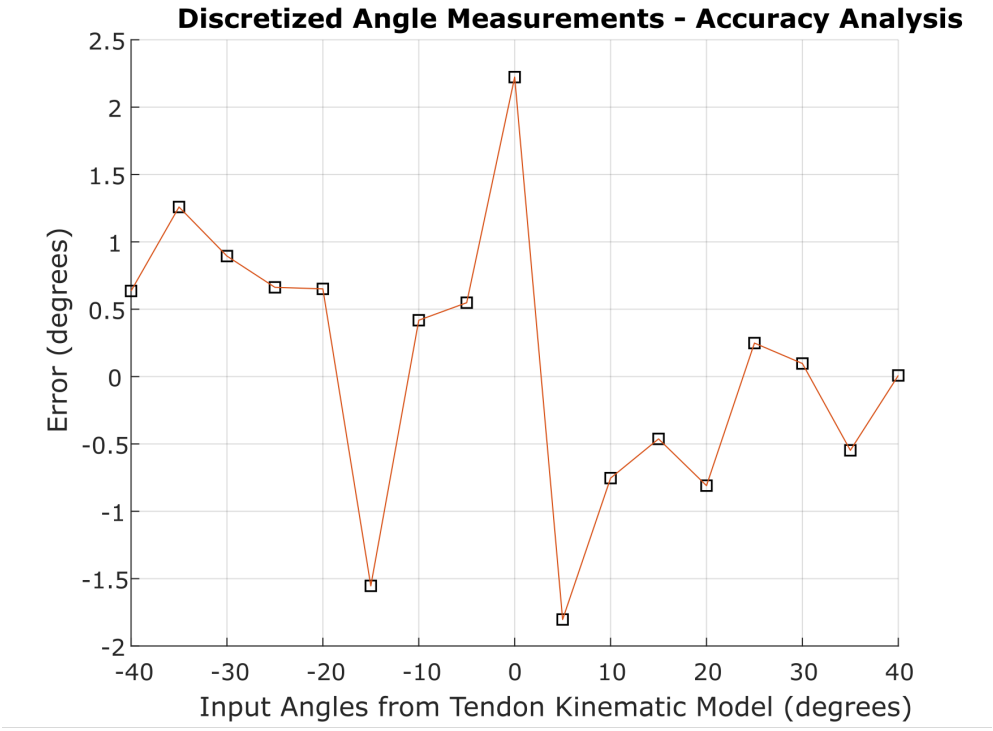


(a)

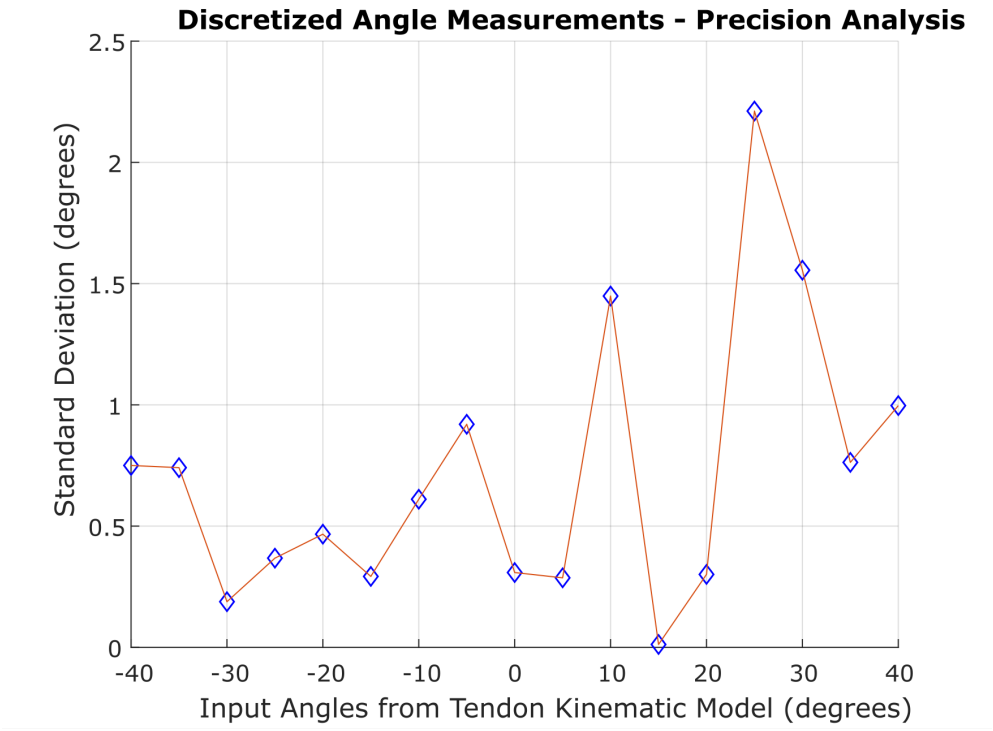


(b)

Figure 6.5: Accuracy and Precision Assessment, (a) Error Plot and (b) Standard Deviation Plot.

### 6.2.1 Calibrated Kinematic Model

The experimental results for the discretized angle measurements showed the poor performance of our tendon kinematic model. We had derived the model with the intention of using it as an input actuation map but the performance evaluation results show that it is unfit to be used as our input signal. With any control system if the input signal is prone to error the control action i.e. the control signal will also be erred. This will results in a poor control system with the output not converging to the desired state, in fact in the worst case the system response may diverge. To address this problem we propose to fit linear regression models to the data from our EM sensor and ArUco marker-based vision algorithm. This makes sense since the results in Fig. 6.4 show the different sensor data points approximating a line. These regression models correlate the change in tendon length, $\Delta L$ with the joint angle, $\theta$ and substitute as a calibrated input actuation map for the derived tendon kinematic model. Also, there can always be several manufacturing errors that can't be appropriately modeled, such as unbalanced pre-tension and misalignment of tendons, etc., for which a fitted/calibrated kinematic model can be a practical solution. The slope $m$ and the y-intercept $b$ of the equation of the best fit line for our model is obtained using regression analysis on a set of bivariate numeric data points. Mathematically they are defined as follows

$$m = \frac{\bar{x}\bar{y} - \overline{xy}}{(\bar{x})^2 - \overline{x^2}} \tag{6.3}$$

$$b = \bar{y} - m\bar{x} \tag{6.4}$$

where $\bar{x}$ is the mean of the x-coordinates of the data points, $\bar{y}$ is the mean of the y-coordinates of the data points, $\overline{xy}$ is the mean of the product of the xy coordinates of the data points and $\overline{x^2}$ is the mean of the squares of the x-coordinates of the data points. Note that this sort of modeling will be specific to each plasma robot and linear fits need to be found for all of them and for each motor separately. The results of our linear regression fit for positive angles subtended by motor 2 is shown in Fig. 6.6 and the fit for negative angles subtended by motor 1 is shown in Fig. 6.7.

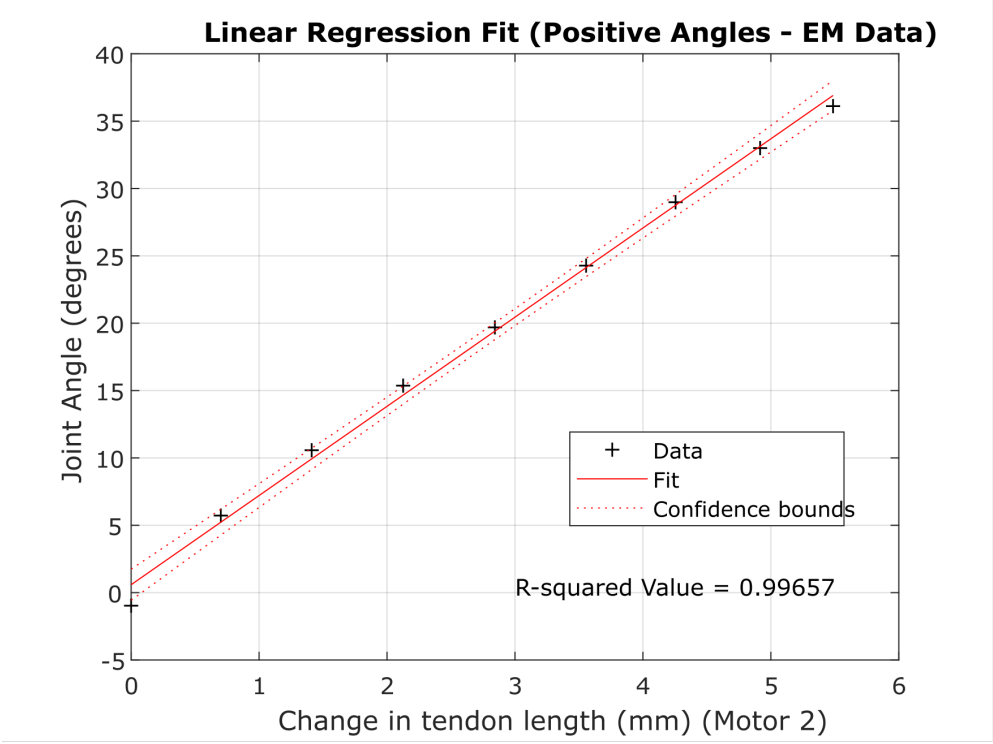


(a)

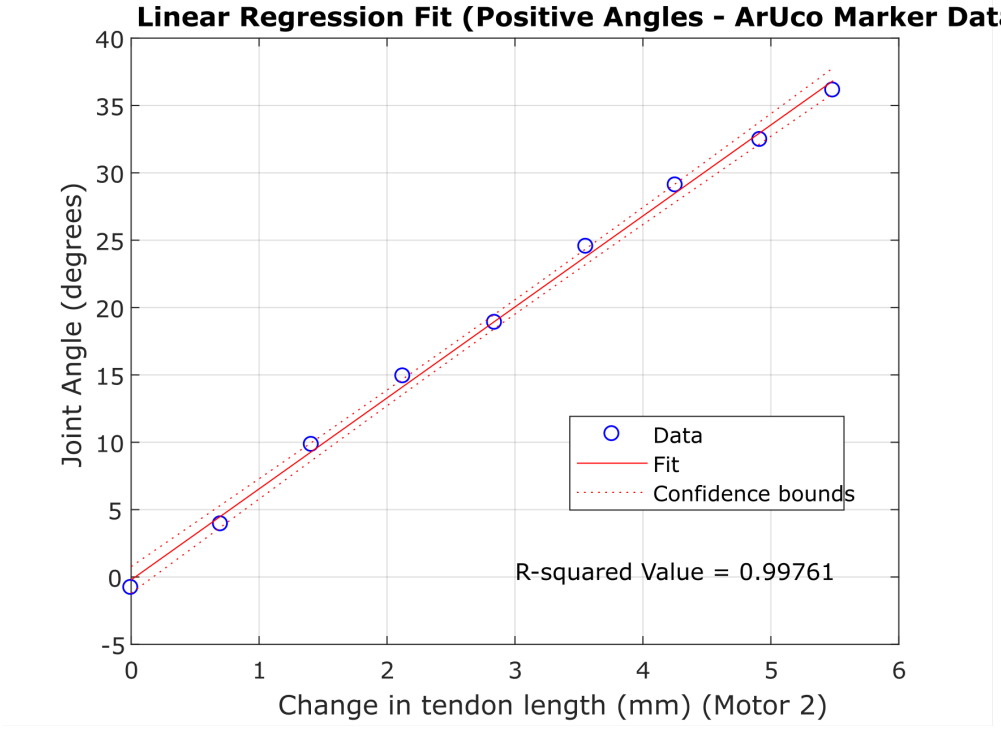


(b)

Figure 6.6: Regression fits to positive angles subtended by Motor 2, (a) EM Sensor data and (b) Aruco Marker based Vision System data.

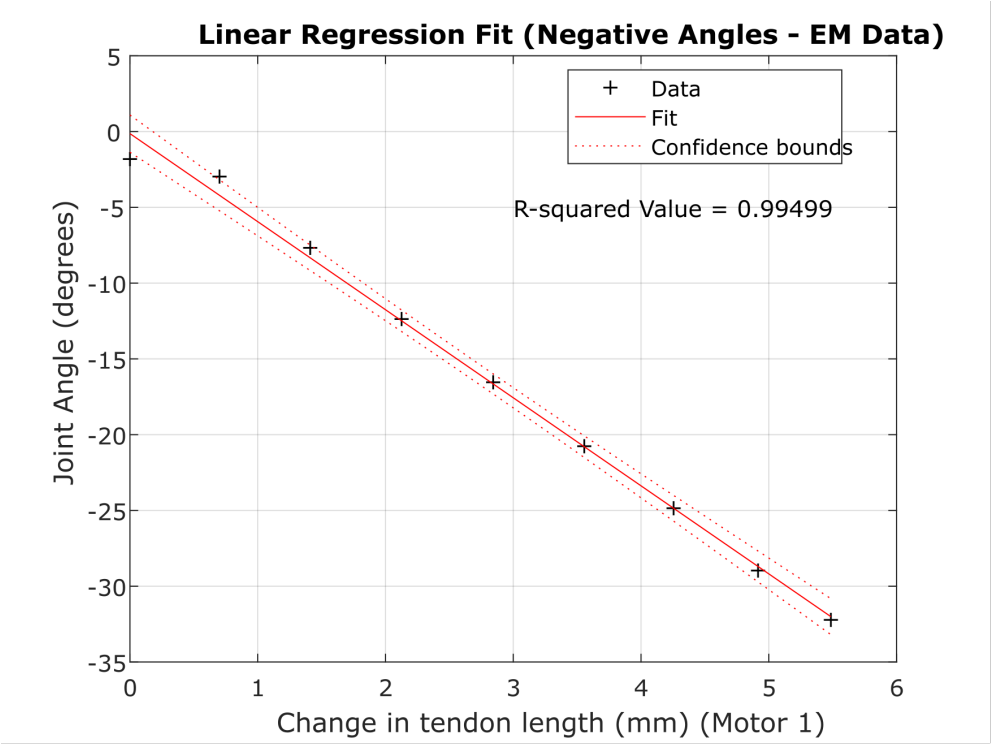


(a)

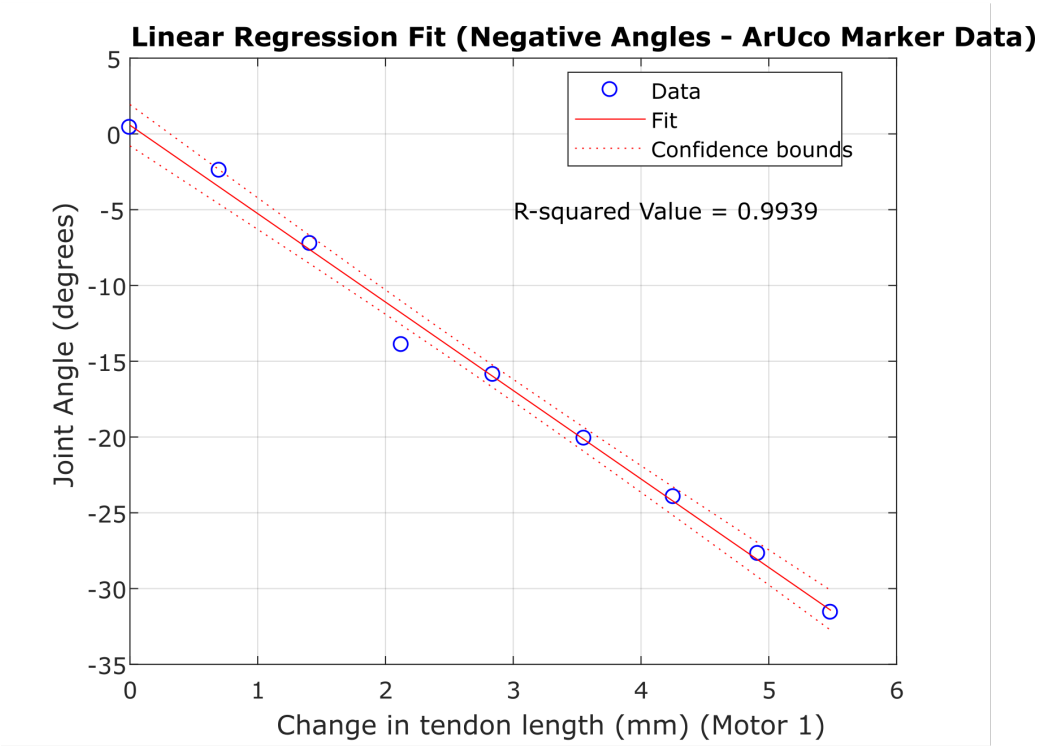


(b)

Figure 6.7: Regression fits to negative angles subtended by Motor 1, (a) EM Sensor data and (b) Aruco Marker based Vision System data.

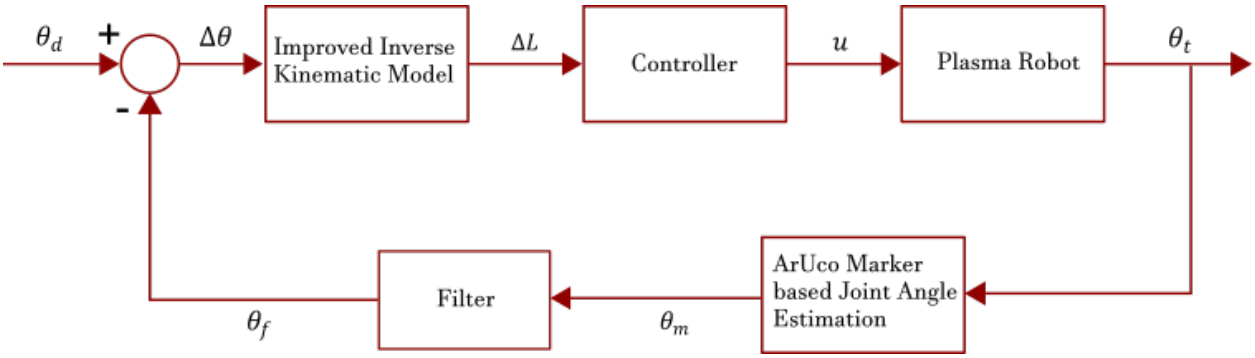


Figure 6.8: Block diagram of the proposed control scheme for the plasma robot with an improved kinematic model.

The quality of our regression fit models was ascertained by calculating the $R^2$ values, also known as the coefficient of determination. $R^2$ value indicates what percent of the prediction error in the y variable is eliminated when the least squares regression is applied to the x variable. Mathematically it is calculated as follows

$$R^2 = 1 - \frac{SE_{line}}{SE_{\bar{y}}} \tag{6.5}$$

where $SE_{line}$ is the sum of squared errors of each data point from the corresponding predicted points on the regression line and $SE_y$ is the sum of squared errors of each data point from $\bar{y}$. A good linear fit will result in data points close to the line of best fit and hence $SE_{line}$ will be close to zero. This, in turn, will yield a value of $R^2$ close to one. In fact, the maximum value that a coefficient of determination can have is one. For all four regression fits the $R^2$ values we obtained were very close to one as displayed on the plots in Fig. 6.6 and Fig. 6.7. This showed a good linear fit and based on these results we propose to use the regression models from fitting the EM sensor data as our new input actuation map. The EM sensor data was used for this purpose because the EM sensor is more accurate than our ArUco marker-based vision system. Also shown in the figures are the 95% confidence bands for our regression fits. For any regression fit model, the slope and the y-intercept will vary for different samples of the same data and as such the best fit line will also change from sample to sample. A confidence band indicates the range in which the true best

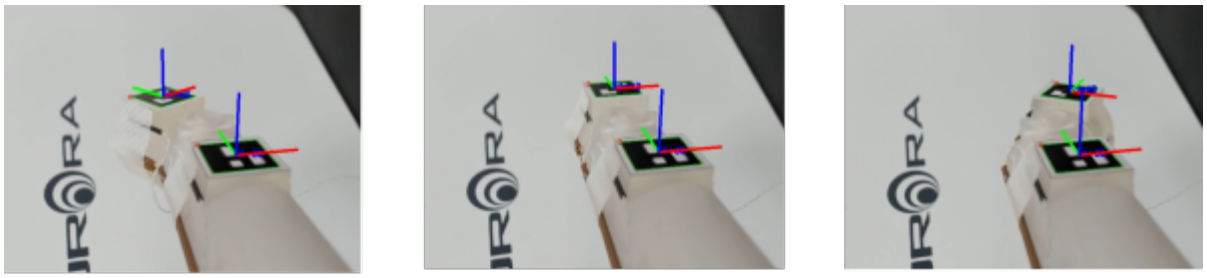

(a) (b) (c)

Figure 6.9: ArUco Marker tracking for Joint Angle Estimation, (a) 0°, (b)Positive extreme and (c)Negative extreme

fit line lies. The confidence bands shown on the plots in Fig. 6.5 and Fig. 6.6 encompass the region which has a 95 % chance of containing the true best fit line. With this improved kinematic model we then proposed a closed loop control structure for our plasma robot as shown by the block digram in Fig. 6.8.

### 6.3 Real Time Continuous Angle Measurements

The second experiment was conducted to validate real-time continuous joint angle measurements from our vision system. To validate the real-time performance of our proposed approach, joint angle readings from ArUco marker-based vision system were compared against those obtained from the EM sensor. The experiment was carried out by continuously actuating the servo motors to which the tendons were connected. A continuous real-time angular displacement from 0° to approximately 160° was applied to each of the servo motors. This corresponded to two cycles of the tip movement across its entire range motion. The experimental setup for this experiment is the same as shown in Fig. 6.3. Stills of the marker tracking in real time at different angles are shown in Fig. 6.9. The EM sensor is operated at a fixed rate of 40 fps whereas the vision system operates at approximately 4 fps to 8 fps. To account for the varying frame rate on our vision system we used the Chrono library to record the time taken to capture each frame. The results from both, the EM sensor and the vision-based approach are presented in Fig. 6.10. The plots of the data from two sensors shown in Fig. 6.10 shows that the results from our approach are in close

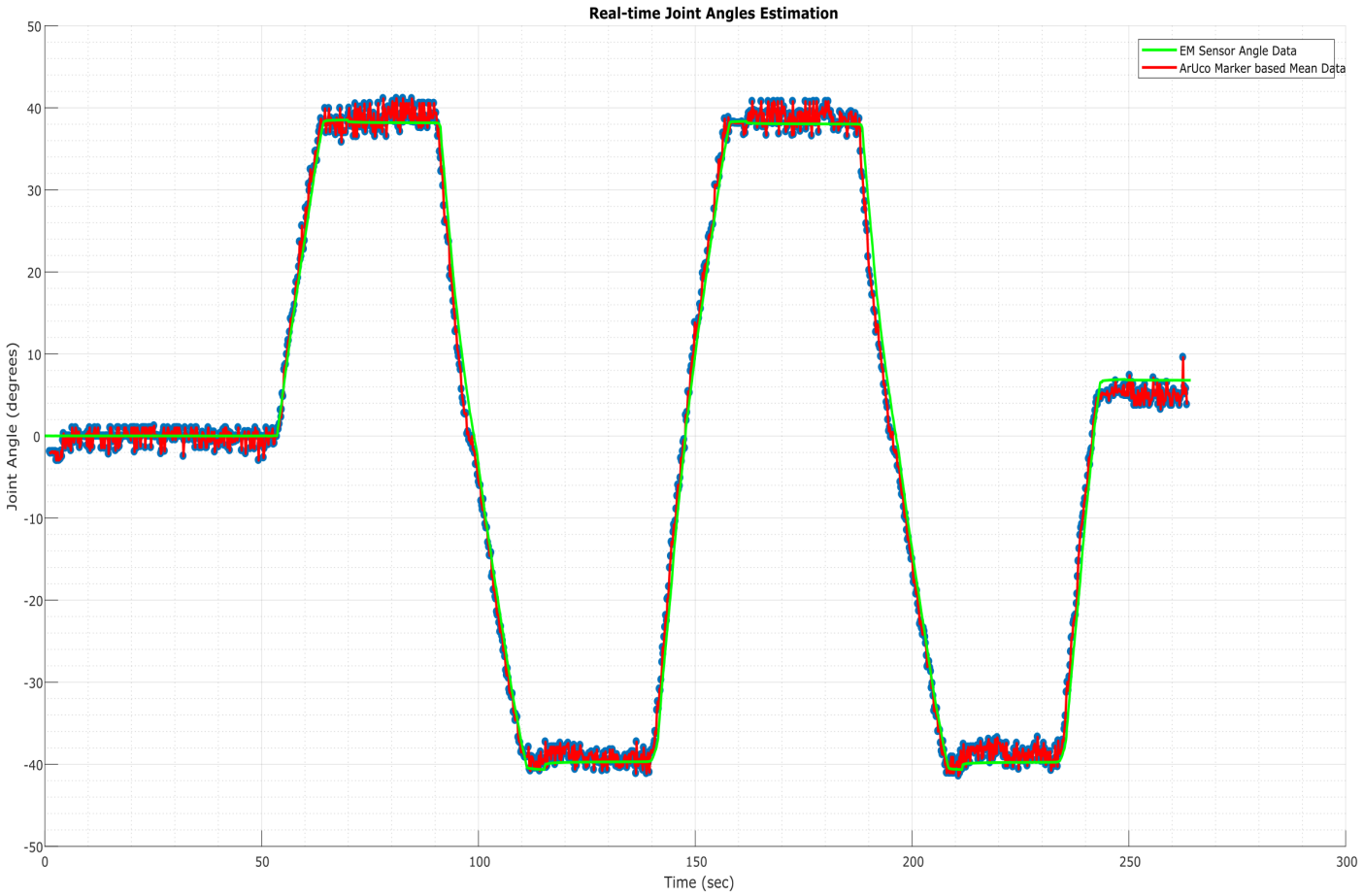


Figure 6.10: Continuous Real Time Joint Angle Measurements.

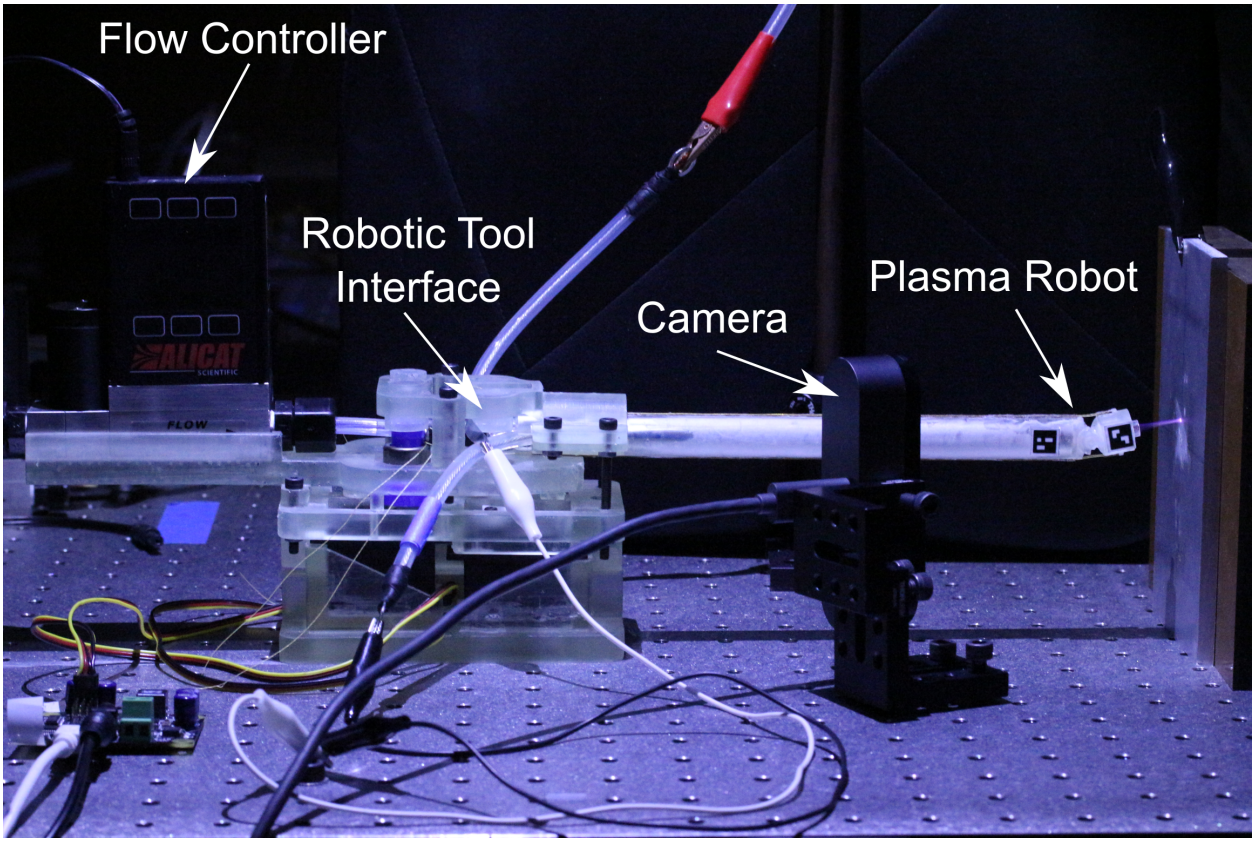


Figure 6.11: Experimental Setup for experiment 3.

agreement with the data obtained from the EM sensor. This is especially true for when the distal tip is moving. With the distal tip static, the data from our vision system is much noisier as compared to the EM sensor. The maximum error at these intervals is noted to be a little more than 2° which is what was expected from the discretized angle measurement experiment. To address this noise we propose the use of a data smoothening filter such as a Gaussian filter but this analysis is left for future studies for now. There is no lag between the two data sets which shows that the ArUco marker-based vision system matches the speed performance of the EM sensor.

### 6.4 Angle measurements with an Active Plasma Plume

To evaluate the performance of our approach in the presence of an active plasma plume which generates EM fields we performed a third experiment. The AruCo marker-based system was used to determine joint angles when the robotic plasma device generated and directed an active plasma

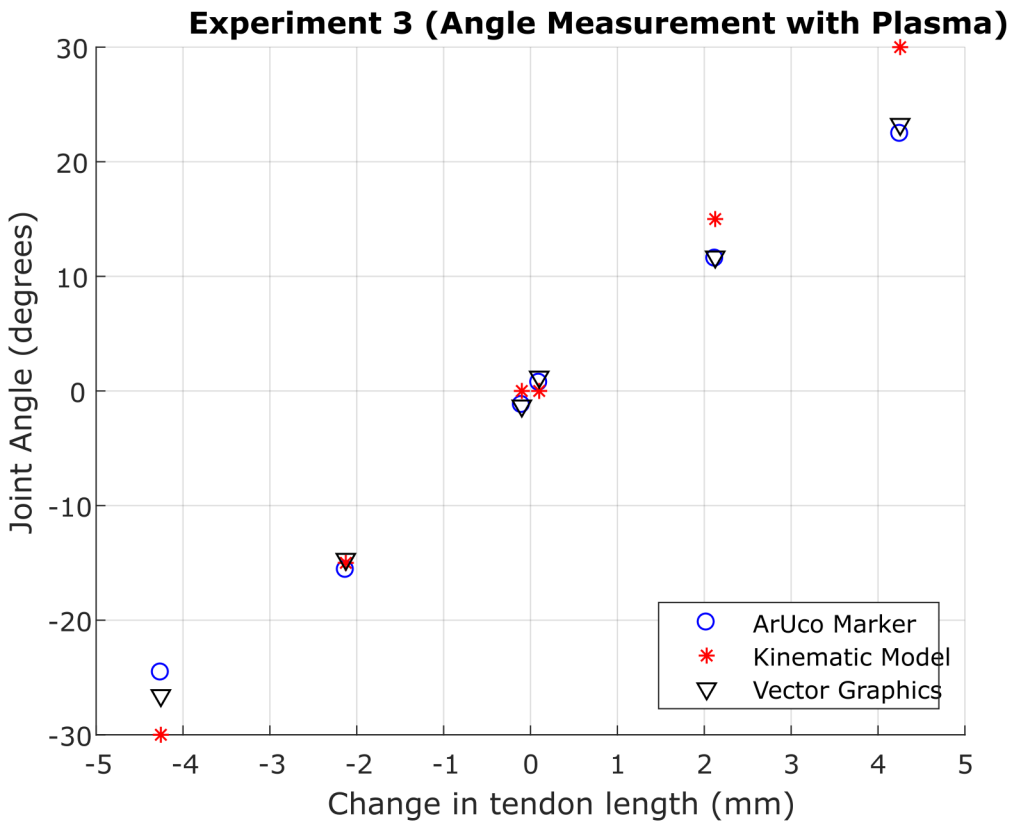


Figure 6.12: Discretized Angle Measurements with an Active Plasma Plume

plume through its distal tip. No EM sensor was used for validation of our results since it is sensitive to EM fields from the plasma. We relied only on the vector graphics approach for validation and validated only a series of discretized joint angle measurements. The experiment consisted of pulling the tendons for different displacements using two servo motors just like the discretized angle measurement experiment. These tendon displacements corresponded to the following set of angular displacements at the robot tip; -30°, -15°, 0°, 15° and 30°. The experimental setup for this experiment is shown in Fig. 6.11.

The results of this experiment are shown in Fig. 6.12. The negative change in tendon length represents actuation by motor 1 which subtends negative angles at the tip whereas a positive change in tendon length represents actuation by motor 2. Note that just like experiment 1, the angle measurements from ArUco marker-based system are close to the measurements from the vector

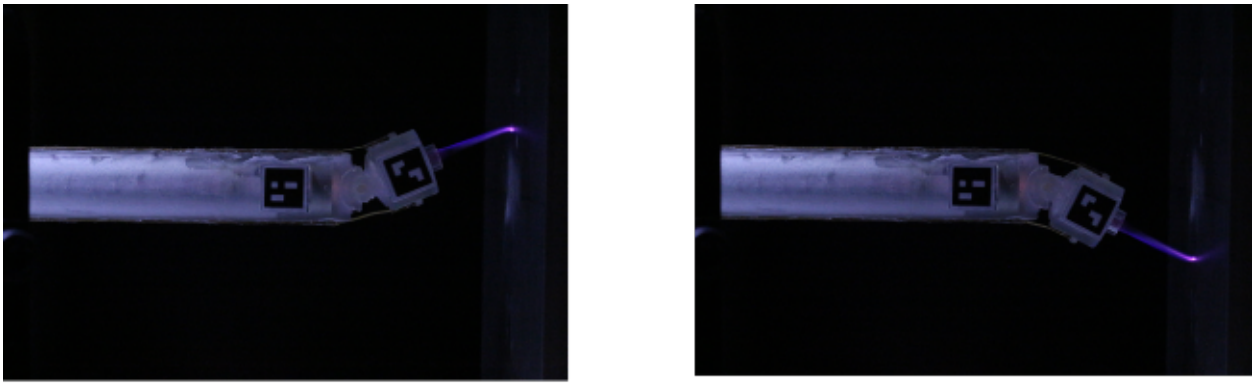

(a) (b)

Figure 6.13: Images for Vector Graphics approach (a) 35° and (b) -35 °.

graphics approach. This corroborates our initial claim that an ArUco marker based joint angle estimation is robust to any EM fields generated by the plasma. The errors in measurements from vector graphics approach and our marker-based approach are again due to the image plane not being parallel to the plane of motion. Fig. 6.13 shows two images that were used for our vector graphics approach. And just like the first experiment the tendon model again performed poorly and the same reasoning holds for this case as well.

# 7. CONCLUSION

In this thesis we proposed an optical marker based vision approach to joint angle estimation of robotic plasma medicine devices. The optical markers used for this study were ArUco markers. We devised and evaluated the ArUco marker based vision algorithm and tested it's performance against other measurement techniques. The results showed that ArUco markers are able to estimate joint angles with an accuracy of $\pm$ 2° and the results were in close proximity to those obtained from the EM sensor. However the measurements from our approach lacked precision and for static tip angles the measurements were very noisy. We recommend the use of a data smoothening filter to address this problem. Other than the EM sensor our proposed algorithm outperformed the tendon kinematic model and vector graphics approach. With regards to the poor performance of the derived tendon kinematic model we explored regression fits to our EM sensor data as an alternative input actuation map. And lastly, as predicted our approach was found to be robust to EM fields and ferromagnetic materials present within the device's vicinity.

In future works, controller performance will be evaluated to ascertain any inherent errors in the robotic tool interface of the plasma robot. This will help us better understand the underlying sources of errors responsible for the poor performance of the tendon kinematic model and will also assist us in designing more accurate actuation schemes for our robot. Other than that, in all our future endeavors marker occlusion will be taken into account. We anticipate that once this device gets introduced to clinical trials it is highly likely that markers may get occluded because of blood smearing. Also, marker occlusion may occur due to the roll of the device itself. To develop robust sensing modalities it is necessary that such occlusion is accounted for. We would also like to improve our algorithm for measuring angles of devices having more than 1 DOF. A possible solution to these anticipated challenges is the use of an ArUco marker map. This would consist of a marker strip with ArUco markers scattered on it and we propose to attach such strips across all joints among such devices. With a large number of distinct ArUco markers occlusion becomes unlikely. However, this would require us to adapt ArUco markers to curved surfaces and with

this, we can also get rid of the square platforms with sharp edges that are not suited for medical procedures.

REFERENCES


[1] G. Fridman, G. Friedman, A. Gutsol, A. B. Shekhter, V. N. Vasilets, and A. Fridman, "Applied plasma medicine," *Plasma Processes and Polymers*, vol. 5, no. 6, pp. 503–533.

[2] B. McKinney, W. McKinney, S. Pattanshetti, and S. C. Ryu, "Feasibility study of in vivo robotic plasma medicine devices," *IEEE International Symposium On Medical Robotics*, 2019.

[3] B. Mittelstadt, P. Kazanzides, J. Zuhars, B. Williamson, P. Cain, F. Smith, and W. Bargar, "The evolution of a surgical robot from prototype to human clinical use," *Computer Integrated Surgery*.

[4] S. Jiang, J. Lou, Z. Yang, J. Dai, and Y. Yu, "Design, analysis and control of a novel tendon-driven magnetic resonance-guided robotic system for minimally invasive breast surgery," *Proceedings of the Institution of Mechanical Engineers, Part H: Journal of Engineering in Medicine*, vol. 229, no. 9, pp. 652–669, 2015. PMID: 26334035.

[5] E. Lugez, H. Sadjadi, D. R. Pichora, R. E. Ellis, S. G. Akl, and G. Fichtinger, "Electromagnetic tracking in surgical and interventional environments: usability study," *International journal of computer assisted radiology and surgery*, vol. 10, pp. 253–262, March 2015.

[6] A. M. Franz, T. Haidegger, W. Birkfellner, K. Cleary, T. M. Peters, and L. Maier-Hein, "Electromagnetic tracking in medicine - a review of technology, validation, and applications," *IEEE Transactions on Medical Imaging*, vol. 33, pp. 1702–1725, Aug 2014.

[7] N. J. van de Berg, D. J. van Gerwen, J. Dankelman, and J. J. van den Dobbelsteen, "Design choices in needle steering - a review," *IEEE/ASME Transactions on Mechatronics*, vol. 20, pp. 2172–2183, Oct 2015.

[8] M. Allan, S. Ourselin, D. Hawkes, J. Kelly, and D. Stoyanov, "3-d pose estimation of articulated instruments in robotic minimally invasive surgery," *IEEE Transactions on Medical*

*Imaging*, vol. 37, pp. 1204–1213, 5 2018.

[9] P. Edgcumbe, C. Nguan, and R. Rohling, "Calibration and stereo tracking of a laparoscopic ultrasound transducer for augmented reality in surgery," in *Augmented Reality Environments for Medical Imaging and Computer-Assisted Interventions* (H. Liao, C. A. Linte, K. Masamune, T. M. Peters, and G. Zheng, eds.), (Berlin, Heidelberg), pp. 258–267, Springer Berlin Heidelberg, 2013.

[10] P. Pratt, A. Jaeger, A. Hughes-Hallett, E. Mayer, J. Vale, A. Darzi, T. Peters, and G.-Z. Yang, "Robust ultrasound probe tracking: initial clinical experiences during robot-assisted partial nephrectomy," *International Journal of Computer Assisted Radiology and Surgery*, vol. 10, pp. 1905–1913, Dec 2015.

[11] L. Zhang, M. Ye, P.-L. Chan, and G.-Z. Yang, "Real-time surgical tool tracking and pose estimation using a hybrid cylindrical marker," *International Journal of Computer Assisted Radiology and Surgery*, vol. 12, pp. 921–930, Jun 2017.

[12] Y. Wu and Z. Hu, "Pnp problem revisited," *Journal of Mathematical Imaging and Vision*, vol. 24, pp. 131–141, Jan 2006.

[13] M. Sato, M. Koizumi, T. Hino, Y. Takahashi, N. Nagashima, N. Itaoka, C. Ueshima, M. Nakata, and Y. Hasumi, "Exploration of assistive technology for uniform laparoscopic surgery," *Asian Journal of Endoscopic Surgery*, vol. 11, no. 4, pp. 325–328.

[14] M. Sato, M. Koizumi, K. Inaba, Y. Takahashi, N. Nagashima, H. Ki, N. Itaoka, C. Ueshima, M. Nakata, and Y. Hasumi, "Auto-tracking camera for dry-box laparoscopic training," in *New Horizons in Laparoscopic Surgery* (M. F. Ferhatoglu, ed.), ch. 6, Rijeka: IntechOpen, 2018.

[15] M. Koeda, D. Yano, N. Shintaku, K. Onishi, and H. Noborio, "Development of wireless surgical knife attachment with proximity indicators using aruco marker," in *Human-Computer Interaction. Interaction in Context* (M. Kurosu, ed.), (Cham), pp. 14–26, Springer International Publishing, 2018.

[16] S. Garrido-Jurado, R. Muñoz-Salinas, F. J. Madrid-Cuevas, and M. J. Marín-Jiménez, "Automatic generation and detection of highly reliable fiducial markers under occlusion," *Pattern Recognition*, vol. 47, no. 6, pp. 2280–2292, 2014.

[17] NDI Europe GmbH, *Aurora V3 User Guide with Window FG*.